

TRAJECTORY-BASED RBF COLLOCATION METHOD FOR SURFACE ADVECTION-DIFFUSION EQUATIONS*

XIAOBIN LI [†], LEEVAN LING [‡], AND YIZHONG SUN [§]

Abstract. We introduce a Trajectory-Based RBF Collocation (TBRBF) method for solving surface advection-diffusion equations on smooth, compact manifolds. TBRBF decouples advection and diffusion by applying a characteristic treatment with a Kansa-type RBF collocation method for diffusion PDE, which yields an operator-split characteristic (OSC) system comprising a characteristic ODE and a diffusion PDE. We rigorously prove the equivalence between the OSC system and the original surface PDE on manifolds by embedding the latter into a narrow band domain. Using an intrinsic approach, we construct a time-continuous embedded PDE with push-forward operators in each chart of the atlas and establish its equivalence with the OSC system in the narrow band. Restricting the solution back to the manifold recovers the OSC system on manifolds, ensuring that the method introduces no operator splitting error. Extensive numerical experiments confirm the robust stability and accuracy of the proposed method.

Key words. Characteristic curve trajectory, Kansa-type RBF collocation method, Surface advection-diffusion equation, Embedded PDE, Push-forward operator

AMS subject classifications. 65M60, 65M12, 65D30, 41A30

1. Introduction. The transport and dispersion of scalar quantities on curved surfaces pose challenges in computational mathematics, with applications ranging across geophysical fluid dynamics, oceanography, biological systems, and materials science [1, 2]. In these fields, it is crucial to extend the classical advection-diffusion framework to accommodate the intrinsic curvature and geometry of the domain, which requires the formulation of the surface advection-diffusion equation.

Consider a closed, compact, oriented C^2 manifold \mathcal{M} of codimension 1 embedded in \mathbb{R}^d . In this work, we focus on the case $d = 3$, as the case $d = 2$ only requires adapting certain components of the results for $d = 3$. The unit outward-pointing normal vector at any point $\mathbf{p} \in \mathcal{M}$ is denoted by $\hat{\mathbf{N}}(\mathbf{p})$, and the tangent space at that point is represented by $\mathcal{T}_{\mathcal{M}}(\mathbf{p})$. The surface advection-diffusion equation posed on the manifold \mathcal{M} takes the form

$$(1.1) \quad \begin{cases} \frac{\partial}{\partial t}u + \mathbf{v}_{\mathcal{M}} \cdot \nabla_{\mathcal{M}}u = \varepsilon \Delta_{\mathcal{M}}u & \text{on } \mathcal{M} \times [0, T], \\ u(\cdot, 0) = u_{\mathcal{M}, 0} & \text{on } \mathcal{M}, \end{cases}$$

where $u(\mathbf{p}, t)$ is the scalar quantity, and $\varepsilon > 0$ is the diffusion coefficient. The tangential velocity field $\mathbf{v}_{\mathcal{M}} : \mathcal{M} \times [0, T] \rightarrow \mathcal{T}_{\mathcal{M}} \subset \mathbb{R}^d$ defines the advection transport along the manifold. In addition, the velocity field is assumed to have the following regularity

$$(1.2) \quad \mathbf{v}_{\mathcal{M}} \in C^0([0, T]; C^{k+1}(\mathcal{M})).$$

* Submitted to

Funding: This work was supported by the General Research Fund (GRF No.12301021, 12300922, 12301824) of Hong Kong Research Grant Council.

[†]Department of Mathematics, Hong Kong Baptist University, Kowloon Tong, Hong Kong (lixiaobin@hkbu.edu.hk).

[‡]Department of Mathematics, Hong Kong Baptist University, Kowloon Tong, Hong Kong (lling@hkbu.edu.hk).

[§]Department of Mathematics, Hong Kong Baptist University, Kowloon Tong, Hong Kong (bill950204@126.com & yzsun95@hkbu.edu.hk).

The manifold gradient operator $\nabla_{\mathcal{M}}$ and the Laplace-Beltrami operator $\Delta_{\mathcal{M}}$ in (1.1) are defined extrinsically as

$$\nabla_{\mathcal{M}} := \mathcal{P}\nabla, \quad \Delta_{\mathcal{M}} := \nabla_{\mathcal{M}} \cdot \nabla_{\mathcal{M}} = (\mathcal{P}\nabla) \cdot (\mathcal{P}\nabla),$$

with the orthogonal projector $\mathcal{P} = \mathcal{P}(\mathbf{p}) := \mathbf{I} - \hat{\mathbf{N}}(\mathbf{p})\hat{\mathbf{N}}(\mathbf{p})^T$, which projects vectors from \mathbb{R}^d at $\mathbf{p} \in \mathcal{M}$ to the tangent space $\mathcal{T}_{\mathcal{M}}(\mathbf{p})$.

For surface advection or advection-diffusion equations, various numerical methods have emerged, with significant attention paid to finite element method [3, 4, 5, 6], meshfree radial basis function (RBF) methods [7, 8], closest point methods [9, 10, 11], and embedding methods [12, 13]. Both closest point and embedding methods rely heavily on using points from a narrow band surrounding the surface to approximate derivative operators, which requires enforcing constant-along-normal (CAN) properties at every time step. Additionally, classical closest point methods only satisfy the CAN property at a fixed time, necessitating interpolation back onto the surface after obtaining information from neighboring points at each step, thus increasing computational complexity. Recently, research on the advection equation [12, 13] has introduced innovative strategies, namely a time-continuous embedding method or a push-forward operator, that extend the tangential flux vector from the surface into the narrow band. This extension ensures that the CAN property is maintained continuously, enabling the direct solution of embedded PDEs without the need for repeated interpolation. However, there has been limited investigation into extrinsic meshfree methods that approximate these surface derivative operators directly.

To guarantee unconditional stability and work well for advection-dominated problems, a widely used strategy for handling the advection term involves trajectory-based approaches, such as characteristic methods [6] or semi-Lagrangian schemes [14, 15, 16], which track the evolution of the solution along flow trajectories. In the context of surface advection equations, [14, 15] integrate RBF-FD discretizations with semi-Lagrangian methods, allowing information at backtracked points to be interpolated from neighboring points, leveraging the CAN property. However, when such methods are extended to solve advection-diffusion equations on manifolds, it becomes necessary to evaluate the Laplace-Beltrami operator. In [16], the authors employ the RBF partition of unity closest point method for advection-diffusion PDE. However, the closest point method presented in [16] satisfies the CAN property only at a fixed time step, necessitating interpolation back onto the surface at each time step, as similarly discussed in [12]. These issues highlight the need for a time-continuous embedding approach or a push-forward diffusion tensor to ensure a consistent and robust treatment of the CAN property throughout the computational process.

As an alternative, we propose a trajectory-based RBF collocation (TBRBF) method to solve surface advection-diffusion equations. This method integrates Kansa-type RBF collocation with a trajectory-based framework, improving stability and flexibility on irregular manifolds. By directly handling the Laplace-Beltrami operator on the manifold, the TBRBF method eliminates the need for repeated interpolation in a narrow band and avoids the drawbacks associated with classical closest point methods that require the CAN property during backtracking interpolation. As a result, the TBRBF method significantly reduces computational complexity while enhancing computational accuracy. In computational physics and numerical PDE literature, the combined system consisting of a characteristic ODE and a diffusion PDE derived from trajectory-based processing is precisely termed an operator-split characteristic (OSC) system. However, the equivalence between the OSC system on manifolds and the original surface advection-diffusion equations has not been sufficiently explored. Previous

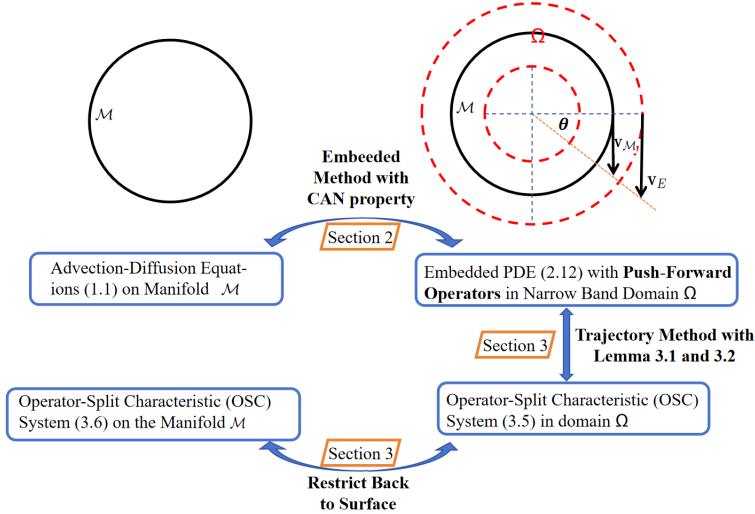


Fig. 1: Schematic diagram illustrating the equivalence between the surface PDE (1.1) and the operator-split characteristic (OSC) system (3.6). On the left, the original surface PDE (1.1) and the OSC system (3.6) are defined on the manifold \mathcal{M} , depicted as a circle. To establish the analytical equivalence, the manifold is embedded into the narrow band domain Ω on the right. In this embedding process, push-forward operators (e.g., velocity \mathbf{v}_E) are employed to derive the embedded PDE (2.16). After proving the equivalence of the embedded PDE (2.16) and the OSC system (3.5) in Ω , restrict (3.5) back to the manifold for the final result (3.6).

studies [17, 18] have provided analyses of the flat geometry counterpart in a bounded domain, and we aim to extend them to manifolds. In our work, we embed the original equation into a narrow band and rigorously establish a time-continuous embedded advection-diffusion equation with push-forward velocity and diffusion tensor in each chart of the atlas. Subsequently, we prove its equivalence with the OSC system in the narrow band domain and finally restrict back to the manifold. Note that the equivalence established above holds in the time-continuous setting, thereby eliminating any operator splitting error. As a result, the classical closest point method is not feasible, which motivates the introduction of push-forward operators. The complete schematic transformation is depicted in Figure 1. Thus, we present a theoretically robust and computationally efficient framework for addressing surface PDEs.

The rest of the paper is structured as follows. In Section 2, we first construct an advection-aligned orthonormal frame and introduce some preliminary information about the intrinsic approach in each chart of the atlas. Then define an embedded advection-diffusion equation with a specifically designed push-forward velocity and diffusion tensor, ensuring that the embedded solution possesses the CAN property over time. Section 3 develops a trajectory-based formulation that establishes the equivalence between the embedded PDE and OSC system in the narrow band domain. We then restrict this formulation back to the surface to obtain the OSC system on the manifold. In Section 4, we detail a Kansa-type RBF collocation algorithm with various time discretization orders, and in Section 5, we present numerical experiments that demonstrate the robust stability and accuracy of the proposed TBRBF method. Finally, Section 6 concludes the paper and outlines directions for future research.

2. The Embedded Advection-Diffusion Equations with Push-Forward Operators. To establish the analytical equivalence between the surface PDE (1.1) and the OSC system on the manifold \mathcal{M} , as illustrated in Figure 1, we begin by embedding the manifold \mathcal{M} into an extended narrow band domain Ω . A key requirement for this embedding is that the resulting PDE preserves the CAN property over time, following the rationale used for pure advection equations in [12, 13]. This leads us to formulate an embedded advection-diffusion equation with push-forward velocity field and diffusion tensor, ensuring that the key dynamical features of the original system are faithfully maintained within the narrow band framework.

While the push-forward velocity we derive in (2.17) agrees with the result in [13] for pure advection, their level set approach may not readily extend to the diffusion tensor. Similarly, the work on curves in [12] may lack rigor when extended to surfaces, especially when the advection velocity is not aligned with a principal direction. Motivated by these limitations, we construct an advection-aligned orthonormal frame and adopt an intrinsic approach within each chart of the atlas that enables a systematic and continuous derivation of both the push-forward velocity and diffusion tensor.

2.1. Advection-aligned orthonormal frame in each chart of the atlas and intrinsic preliminaries. We begin by constructing a well-defined orthonormal basis for the tangent space $\mathcal{T}_{\mathcal{M}}(\mathbf{p})$ at each point $\mathbf{p} \in \mathcal{M}$, consistent with the geometric structure imposed by the surface PDE (1.1). Specifically, the tangential velocity field $\mathbf{v}_{\mathcal{M}}(\mathbf{p}) \in \mathcal{T}_{\mathcal{M}}(\mathbf{p})$ can be used to define the primary tangent vector $\hat{\mathbf{T}}_1 = \mathbf{v}_{\mathcal{M}}/\|\mathbf{v}_{\mathcal{M}}\|$ for a manifold $\mathcal{M} \in \mathbb{R}^3$. The secondary tangent vector is then determined by $\hat{\mathbf{T}}_2 = (\hat{\mathbf{N}} \times \hat{\mathbf{T}}_1)/\|\hat{\mathbf{N}} \times \hat{\mathbf{T}}_1\|$, with the unit normal vector $\hat{\mathbf{N}}$.

To obtain an appropriate embedded PDE, it is necessary to establish the relationship between the push-forward operators and the operators in the surface equation. Crucially, preserving the CAN property over time requires that the angular velocity of the embedded PDE remains the same, which in turn necessitates working within the same local parameterization. Notably, the constancy of the angular velocity results in a discrepancy between the tangential velocity and $\mathbf{v}_{\mathcal{M}}$, while also causing variations in the diffusion speed throughout the embedding process. These considerations motivate the adoption of an intrinsic approach.

Recall that an atlas \mathcal{A} for a topological space \mathcal{M} is made up of charts, each being a homeomorphism $\Phi : U \subset \mathcal{M} \rightarrow V \subset \mathbb{R}^2$ from an open subset $U \subset \mathcal{M}$ to an open set V in the Euclidean parameter plane, typically denoted by the pair $\{U, \Phi\}$ [19]. In our framework, for each point $\mathbf{p}_0 \in \mathcal{M}$, with advection velocity $\mathbf{v}_{\mathcal{M}}(\mathbf{p}_0, t)$, we select a chart U such that $\mathbf{p}_0 \in U$ and fix the origin of the parameter plane by imposing $\Phi(\mathbf{p}_0) = (0, 0)$. The inverse map $\Gamma = \Phi^{-1}$ is the local surface parameterization for the chart U . Within this chart we denote the coordinates by $(\theta_1, \theta_2) \in V$. The two scalars $\theta_i (i = 1, 2)$ are chosen to measure displacements along the orthonormal tangent directions $\hat{\mathbf{T}}_i$ generated from the given velocity field, i.e.

$$(2.1) \quad \partial_{\theta_1} \Gamma(\theta_1, \theta_2) = \hat{\mathbf{T}}_1, \quad \partial_{\theta_2} \Gamma(\theta_1, \theta_2) = \hat{\mathbf{T}}_2.$$

This construction incorporates the direction of the advection velocity into the coordinate system, making it especially effective for analyzing and discretizing differential operators that emerge from the surface PDE. Since this approach closely resembles a Frenet-Serret frame (TNB), which is based on curves, we refer to our local frame as the **advection-aligned orthonormal frame** $\mathbf{B}_2 := [\hat{\mathbf{T}}_1, \hat{\mathbf{T}}_2, \hat{\mathbf{N}}] \subset \mathbb{R}^3$. While \mathbf{B}_2 is intrinsically defined on \mathcal{M} , our construction naturally extends to the later defined narrow band domain (2.6). A geometric illustration is offered in Figure 2.

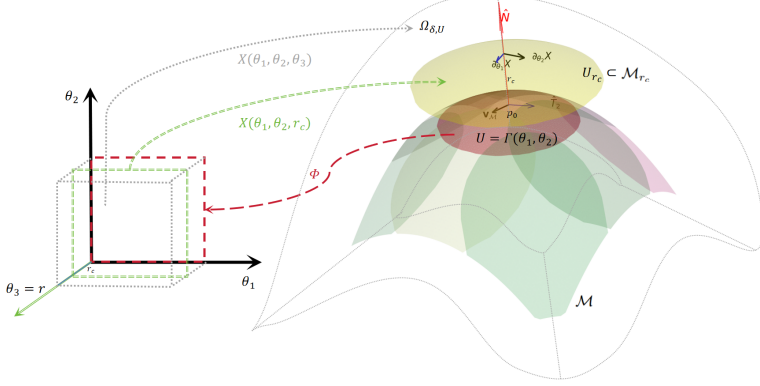


Fig. 2: Construction of a local advection-aligned orthonormal frame on the surface \mathcal{M} using the advection velocity as one tangent vector. The parameter domain V is mapped to the surface via the atlas mapping $\Gamma = \Phi^{-1}$, where (θ_1, θ_2) parametrize the chart U on the surface \mathcal{M} . A third coordinate $\theta_3 = r$ extends the chart off the surface along \hat{N} , producing the narrow-band mapping X (2.10) from $V \times [-\delta, \delta]$ (gray rectangular area) to $\Omega_{\delta, U}$ (gray dotted area), so that each level set $r = r_c := \text{const}$ is a chart U_{r_c} on the parallel surface \mathcal{M}_{r_c} .

As the intrinsic differential operator and related operations will be used, we begin by providing some preliminary information regarding the intrinsic approach. The metric matrix G_Γ of the first fundamental form records the inner product of the first-order partial derivatives of $\Gamma(\theta_1, \theta_2)$

$$(2.2) \quad G_\Gamma = \begin{bmatrix} E & F \\ F & G \end{bmatrix} = \begin{bmatrix} \partial_{\theta_1} \Gamma \cdot \partial_{\theta_1} \Gamma & \partial_{\theta_1} \Gamma \cdot \partial_{\theta_2} \Gamma \\ \partial_{\theta_1} \Gamma \cdot \partial_{\theta_2} \Gamma & \partial_{\theta_2} \Gamma \cdot \partial_{\theta_2} \Gamma \end{bmatrix} = \mathbf{I}.$$

To characterize the curvature of $\mathcal{M} \in \mathbb{R}^3$, we can use the inner product of the second-order partial derivatives of $\Gamma(\theta_1, \theta_2)$ with the unit normal vector \hat{N} to obtain following curvature matrix H_Γ of the second fundamental form

$$(2.3) \quad H_\Gamma = \begin{bmatrix} L & M \\ M & N \end{bmatrix} = \begin{bmatrix} \partial_{\theta_1 \theta_1} \Gamma \cdot \hat{N} & \partial_{\theta_1 \theta_2} \Gamma \cdot \hat{N} \\ \partial_{\theta_1 \theta_2} \Gamma \cdot \hat{N} & \partial_{\theta_2 \theta_2} \Gamma \cdot \hat{N} \end{bmatrix}.$$

Let S_Γ denote the shape operator, which is defined as

$$(2.4) \quad S_\Gamma = G_\Gamma^{-1} H_\Gamma = H_\Gamma.$$

Then, to express the derivatives of the normal vector in the direction of any tangent vector along our advection-aligned coordinate directions, we use the following Weingarten equation

$$(2.5) \quad [\partial_{\theta_1} \hat{N}, \partial_{\theta_2} \hat{N}] = -[\partial_{\theta_1} \Gamma, \partial_{\theta_2} \Gamma] S_\Gamma = -[\partial_{\theta_1} \Gamma, \partial_{\theta_2} \Gamma] \begin{bmatrix} L & M \\ M & N \end{bmatrix}.$$

Next, we embed the original surface PDE (1.1) within a narrow band domain surrounding the manifold \mathcal{M} to obtain the embedded PDE defined below (2.16). The narrow band domain is defined explicitly as follows

$$(2.6) \quad \Omega = \Omega_\delta := \{\mathbf{x} \in \mathbb{R}^d : \|\mathbf{x} - \mathbf{p}\|_{\ell_2(\mathbb{R}^d)} < \delta \text{ for some } \mathbf{p} \in \mathcal{M}\},$$

with respect to a positive tubular radius $\delta \in \mathbb{R}$. Then, the closest point mapping $\text{cp} : \Omega \subset \mathbb{R}^d \rightarrow \mathcal{M}$ can be well-defined in Ω (2.6) for a sufficiently small δ [20], which is constructed as follows

$$(2.7) \quad \text{cp}(\mathbf{x}) = \arg \inf_{\mathbf{p} \in \mathcal{M}} \|\mathbf{p} - \mathbf{x}\|_{\ell^2(\mathbb{R}^d)}, \quad \mathbf{x} \in \Omega.$$

Building on the narrow band domain Ω (2.6), define the signed distance function $r : \Omega \times \mathcal{M} \rightarrow \mathbb{R}$ by

$$(2.8) \quad r = \text{dist}(\mathbf{x}, \text{cp}(\mathbf{x})) := \text{sign}(\hat{\mathbf{N}} \cdot (\mathbf{x} - \text{cp}(\mathbf{x}))) \|\mathbf{x} - \text{cp}(\mathbf{x})\|_{\ell^2(\mathbb{R}^d)}.$$

The parallel surfaces of \mathcal{M} with fixed distance $r = r_c := \text{const}$ can be directly defined

$$(2.9) \quad \mathcal{M}_{r_c} = \{\mathbf{x} \in \Omega : \text{sign}(\hat{\mathbf{N}} \cdot (\mathbf{x} - \mathbf{p})) \|\mathbf{x} - \mathbf{p}\|_{\ell^2(\mathbb{R}^d)} = r_c \text{ for } \mathbf{p} = \text{cp}(\mathbf{x}) \in \mathcal{M}\}.$$

For notational convenience, we set $\theta_3 = r$ and denote $\Omega_{\delta, U} = U \times [-\delta, \delta]$. Using the local coordinate mapping Γ together with the closest point mapping, we define the extended mapping $X : V \times [-\delta, \delta] \rightarrow \Omega_{\delta, U} \subset \Omega$ as

$$(2.10) \quad X(\boldsymbol{\theta}) = \Gamma(\theta_1, \theta_2) + \theta_3 \hat{\mathbf{N}}(\theta_1, \theta_2) \quad \boldsymbol{\theta} = (\theta_1, \theta_2, \theta_3),$$

which is illustrated geometrically in Figure 2. We also have the following properties

$$\text{cp}(X(\boldsymbol{\theta})) = \Gamma(\theta_1, \theta_2), \quad \{X(\theta_1, \theta_2, r_c) : \Gamma(\theta_1, \theta_2) \in U\} \subset \mathcal{M}_{r_c}.$$

Using the Weingarten equation (2.5), we can differentiate $X(\theta_1, \theta_2, \theta_3)$ with respect to θ_i ($i = 1, 2, 3$) to obtain the tangential and normal derivatives as below

$$(2.11) \quad [\partial_{\theta_1} X, \partial_{\theta_2} X, \partial_{\theta_3} X] = [\partial_{\theta_1} \Gamma, \partial_{\theta_2} \Gamma, \hat{\mathbf{N}}] \begin{bmatrix} 1-rL & -rM & 0 \\ -rM & 1-rN & 0 \\ 0 & 0 & 1 \end{bmatrix} := [\hat{\mathbf{T}}_1, \hat{\mathbf{T}}_2, \hat{\mathbf{N}}] \mathbf{R}.$$

Equation (2.11) implies that the frame of X , denoted by \mathbf{B}_3 , is neither parallel to our proposed advection-aligned orthogonal frame \mathbf{B}_2 nor necessarily orthogonal (see Figure 2), since the matrix \mathbf{R} is not a diagonal matrix. This lack of parallelism underscores a significant limitation in applying the method presented by [12] to surfaces when the advection velocity is not aligned with a principal direction. According to the definition of the metric tensor, the components of metric tensor $\mathbf{G}_X(\boldsymbol{\theta})$ associated with X are given by $g_{ij}(\boldsymbol{\theta}) = \partial_{\theta_i} X \cdot \partial_{\theta_j} X$ ($i, j = 1, 2, 3$). Hence, in our constructed frame, the full metric tensor in coordinates $(\theta_1, \theta_2, \theta_3)$ can be expressed as

$$(2.12) \quad \mathbf{G}_X(\boldsymbol{\theta}) = \mathbf{R} \mathbf{R}^T = \begin{bmatrix} (1-rL)^2 + (rM)^2 & -rM(2-r(L+N)) & 0 \\ -rM(2-r(L+N)) & (1-rN)^2 + (rM)^2 & 0 \\ 0 & 0 & 1 \end{bmatrix}.$$

In this study, we employ three mutually related coordinate frames

- Ambient Cartesian frame \mathbf{B}_1 with matrix form $[\mathbf{e}_1, \mathbf{e}_2, \mathbf{e}_3]$.
- Advection-aligned frame \mathbf{B}_2 on a chart $U \subset \mathcal{M}$ with matrix form $[\hat{\mathbf{T}}_1, \hat{\mathbf{T}}_2, \hat{\mathbf{N}}]$.
- Narrow-band frame \mathbf{B}_3 in $\Omega_{\delta, U} \subset \Omega$ with matrix form $[\partial_{\theta_1} X, \partial_{\theta_2} X, \partial_{\theta_3} X]$.

We can use above notation to rewrite the equation (2.11) and (2.12)

$$(2.13) \quad \mathbf{B}_3 = \mathbf{B}_2 \mathbf{R}, \quad \mathbf{G}_X = \mathbf{B}_3^T \mathbf{B}_3.$$

As mentioned above, to localize the analysis, we require an atlas A^* whose coordinates are aligned with the advection field, formalized in the following assumption.

Assumption 1. Let $\mathbf{p}_0 \in \mathcal{M}$ be any point with advection velocity $\mathbf{v}_M(\mathbf{p}_0, t)$ in (1.1), assume an atlas pair $\{U, \Phi\}$ with $\Phi(\mathbf{p}_0) = \mathbf{0}$ and its inverse $\Gamma = \Phi^{-1}$ satisfying the advection alignment (2.1) under the advection-aligned frame \mathbf{B}_2 . The chart U extends to a narrow band $\Omega_{\delta, U} \supset U$ by X in (2.10). For each $r_c \in (-\delta, \delta)$, set $\mathbf{x}_0 = X(0, 0, r_c)$ so that $\text{cp}(\mathbf{x}_0) = \mathbf{p}_0$. Moreover, all operators admit equivalent representations in any frames via (2.13).

Building on the preceding preliminaries of the intrinsic approach, let atlas A^* satisfy Assumption 1 and denote a scalar function $u_E(\mathbf{x})$ in \mathbf{B}_1 . Then, we can transform $u_E(\mathbf{x})$ from \mathbf{B}_1 coordinate to \mathbf{B}_3 coordinate as $u_E(\mathbf{x}) \circ X := \tilde{u}_E(\boldsymbol{\theta})$. Hence, for the local metric tensor \mathbf{G}_X in (2.12), the gradient operator can be transformed from \mathbf{B}_1 to \mathbf{B}_3 as [3, Eq. (2.2)]

$$(2.14) \quad \nabla u_E(\mathbf{x}) = \sum_{i,j=1}^3 g^{ij} \partial_{\theta_j} \tilde{u}_E(\boldsymbol{\theta}) \partial_{\theta_i} X = \mathbf{B}_3 \mathbf{G}_X^{-1} \nabla_{\theta} \tilde{u}_E(\boldsymbol{\theta}),$$

where the gradient ∇_{θ} in frame \mathbf{B}_3 is defined as $\nabla_{\theta} := [\partial_{\theta_1}, \partial_{\theta_2}, \partial_{\theta_3}]^T$.

2.2. Time-continuous embedded PDE with push-forward operators. We present the following theorem to show the embedded PDE with the push-forward velocity and diffusion tensor.

THEOREM 2.1. Let $\mathcal{M} \in \mathbb{R}^3$ be a closed C^2 , compact, oriented, codimension 1 surface, $u : \mathcal{M} \rightarrow \mathbb{R}$ be the solution of the surface advection-diffusion equation (1.1). At each point $\mathbf{p}_0 \in \mathcal{M}$, choose an atlas A^* with associated chart (U, Φ) satisfying Assumption 1. Then, on the tubular neighborhood $\Omega_{\delta, U} \supset U$, a push-forward velocity field $\mathbf{v}_E : \Omega_{\delta, U} \times [0, T] \rightarrow \mathbb{R}^d$ and a push-forward diffusion tensor $\mathbf{A} : \Omega_{\delta, U} \times [0, T] \rightarrow \mathbb{R}^{d \times d}$ with components a_{ij} ($i, j = 1, 2, 3$) and $a_{ij} = a_{ji}$ ($i \neq j$), such that the constant-along-normal (CAN) extension

$$(2.15) \quad u_E(\mathbf{x}, t) = u(\text{cp}(\mathbf{x}), t) \quad \forall \mathbf{x} \in \Omega_{\delta, U}, t \in [0, T].$$

solves the embedded PDE

$$(2.16) \quad \begin{cases} \frac{\partial}{\partial t} u_E + \mathbf{v}_E \cdot \nabla u_E = \varepsilon \nabla \cdot (\mathbf{A} \nabla u_E), & \text{in } \Omega_{\delta, U}, t \in [0, T], \\ u_E(\cdot, 0) = u(\text{cp}(\cdot), 0), & \text{in } \Omega_{\delta, U}, \\ \partial_{\mathbf{N}} u_E = 0 \quad \text{and} \quad \partial_{\mathbf{N}}^{(2)} u_E = 0, & \text{on } \mathcal{M}, t \in [0, T]. \end{cases}$$

The push-forward operators are given by

$$(2.17) \quad \mathbf{v}_E(\mathbf{x}, t) = \mathbf{R} \mathbf{v}_M(\text{cp}(\mathbf{x}), t) \quad \forall \mathbf{x} \in \Omega_{\delta, U}, t \in [0, T],$$

$$(2.18) \quad \mathbf{A} = \begin{bmatrix} (1 - rN)^2 + (rM)^2 & -rM(2 - r(L + N)) & a_{31} \\ -rM(2 - r(L + N)) & (1 - rL)^2 + (rM)^2 & a_{32} \\ -\int_0^r \left(\sum_{i=1}^2 \partial_{\theta_i} a_{i1} \right) & -\int_0^r \left(\sum_{i=1}^2 \partial_{\theta_i} a_{i2} \right) & a_{33} \end{bmatrix},$$

where \mathbf{R} is defined in (2.11), r denotes the signed distance function (2.8), θ_1, θ_2 are local parametric variables, and L, M, N are related to the second fundamental form (2.3). Moreover, a_{33} is an arbitrary value.

REMARK 2.1. The push-forward velocity given in (2.17) is consistent with the result obtained in [13] for the pure advection equations, which provides an independent validation of our derivation. It is important to emphasize that the off-diagonal components a_{31} and a_{32} of the push-forward diffusion tensor in (2.18) are, in general, nonzero for $r \neq 0$ and vanish only when $r = 0$. This indicates that, in the embedded PDE, material diffusion is not confined to planes parallel to the surface but also incorporates diffusion processes in the normal direction. Such effects cannot be captured by the level set or parallel tangent plane approaches in the existing literature [13, 12].

The enforcement of the CAN property (2.15) ensures that the angular velocity of the embedded PDE is invariant over time. This fundamental requirement motivates the transformation of the governing equations (1.1) (surface advection-diffusion) and (2.16) (embedded PDE) from the Cartesian coordinates into the constructed advection-aligned orthonormal frame. The core idea of our proof is that, by expressing both equations in this intrinsic frame, the coefficients can be directly matched, thereby yielding explicit expressions for the push-forward velocity and the diffusion tensor.

Before proceeding to the proof of Theorem 2.1, we present the following lemma, which provides the transformation of the diffusion term $\nabla \cdot (\mathbf{A}(\mathbf{x}, t) \nabla u_E(\mathbf{x}, t))$ defined in the Cartesian coordinate system \mathbf{B}_1 into the local coordinate system \mathbf{B}_3 .

LEMMA 2.2. Assume all in Theorem 2.1, let $\mathbf{A}_X(\boldsymbol{\theta}, t)$ be the diffusion tensor in the local coordinate system \mathbf{B}_3 , satisfying $\mathbf{A}(\mathbf{x}, t) = \mathbf{B}_3 \mathbf{A}_X(\boldsymbol{\theta}, t) \mathbf{B}_3^{-1}$. The diffusion term $\nabla \cdot (\mathbf{A}(\mathbf{x}, t) \nabla u_E(\mathbf{x}, t))$ under the Cartesian coordinates \mathbf{B}_1 can be expressed as the following intrinsic form in local system \mathbf{B}_3 .

$$\begin{aligned} \nabla \cdot (\mathbf{A}(\mathbf{x}, t) \nabla u_E(\mathbf{x}, t)) = & \nabla_{\boldsymbol{\theta}}^T (\mathbf{B}_3 \mathbf{A}_X(\boldsymbol{\theta}) \mathbf{B}_3^{-1}) \mathbf{B}_3^{-1} \mathbf{B}_3^{-T} \nabla_{\boldsymbol{\theta}} \tilde{u}_E(\boldsymbol{\theta}, t) \\ (2.19) \quad & + \text{Tr} (\mathbf{B}_3^{-T} (\nabla_{\boldsymbol{\theta}} \nabla_{\boldsymbol{\theta}}^T) \tilde{u}_E(\boldsymbol{\theta}, t) \mathbf{B}_3^{-1} (\mathbf{B}_3 \mathbf{A}_X(\boldsymbol{\theta}) \mathbf{B}_3^{-1})). \end{aligned}$$

Proof. Applying the product chain rule for matrix differentiation, the diffusion term $\nabla \cdot (\mathbf{A}(\mathbf{x}, t) \nabla u_E(\mathbf{x}, t))$ can be decomposed into the contraction of the gradient of \mathbf{A} with ∇u_E and the double contraction of \mathbf{A} with the Hessian of u_E , i.e. $\nabla \cdot (\mathbf{A}(\mathbf{x}, t) \nabla u_E(\mathbf{x}, t)) = \nabla (\mathbf{A}(\mathbf{x}, t)) \cdot \nabla u_E(\mathbf{x}, t) + \mathbf{A}(\mathbf{x}, t) : (\nabla \nabla^T) u_E(\mathbf{x}, t)$. Then, using the gradient operator (2.14) and relation $\mathbf{G}_X = \mathbf{B}_3^T \mathbf{B}_3$ in (2.13) to transform coordinates from \mathbf{B}_1 to \mathbf{B}_3 , we can easily obtain (2.19). \square

Proof. (Theorem 2.1) We start by recalling the CAN property (2.15): for any $(\theta_1, \theta_2, \theta_3)$ such that $X(\theta_1, \theta_2, \theta_3) := \mathbf{x} \in \Omega_{\delta, U} \subset \Omega$ and $(\theta_1, \theta_2) := \mathbf{p} = \text{cp}(\mathbf{x}) \in U \subset \mathcal{M}$, the extended solution satisfies $\tilde{u}_E(\boldsymbol{\theta}, t) = u_E(\mathbf{x}, t) = u(\mathbf{p}, t) = \tilde{u}((\theta_1, \theta_2), t)$. This immediately implies that the extended solution u_E depends only on the surface projection. In particular, the first derivatives satisfy

$$(2.20) \quad \partial_{\theta_i} \tilde{u}_E(\boldsymbol{\theta}, t) = \partial_{\theta_i} \tilde{u}((\theta_1, \theta_2), t), \quad i = 1, 2, \quad \partial_{\theta_3} \tilde{u}_E(\boldsymbol{\theta}, t) = 0.$$

Furthermore, we can derive the second derivatives as

$$(2.21) \quad \partial_{\theta_i \theta_j} \tilde{u}_E(\boldsymbol{\theta}, t) = \partial_{\theta_i \theta_j} \tilde{u}((\theta_1, \theta_2), t), \quad i, j = 1, 2, \quad \partial_{\theta_i \theta_3} \tilde{u}_E(\boldsymbol{\theta}, t) = 0, \quad i = 1, 2, 3.$$

Subsequently, we employ the intrinsic approach to transform the embedded PDE (2.16) and surface advection-diffusion equation (1.1) from the Cartesian coordinates to the advection-aligned orthonormal frame. Since the time derivative is independent of the spatial variables, it remains unaffected by this transformation. By using the CAN property (2.15), we get

$$(2.22) \quad \frac{\partial}{\partial t} u_E(\mathbf{x}, t) = \frac{\partial}{\partial t} \tilde{u}_E(\boldsymbol{\theta}, t) = \frac{\partial}{\partial t} \tilde{u}((\theta_1, \theta_2), t) = \frac{\partial}{\partial t} u(\mathbf{p}, t).$$

We then focus on transforming the advection term $\mathbf{v}_E(\mathbf{x}, t) \cdot \nabla u_E(\mathbf{x}, t)$ of the embedded PDE (2.16) into the local coordinate system. To do this, we express the velocity $\mathbf{v}_E(\mathbf{x}, t)$ in the intrinsic frame as $\mathbf{v}_E = \mathbf{B}_3 [\tilde{\mathbf{v}}_E]_{\mathbf{B}_3}$, where $[\cdot]_{\mathbf{B}_3}$ denotes the coordinate representation with respect to the basis \mathbf{B}_3 . Combining with the intrinsic gradient (2.14) and equation (2.13), the original advection term transforms as

$$(2.23) \quad \mathbf{v}_E(\mathbf{x}, t) \cdot \nabla u_E(\mathbf{x}, t) = [\tilde{\mathbf{v}}_E]_{\mathbf{B}_3} \mathbf{B}_3^T \mathbf{B}_3 \mathbf{G}_X^{-1} \nabla_\theta \tilde{u}_E(\boldsymbol{\theta}, t) = [\tilde{\mathbf{v}}_E^T]_{\mathbf{B}_3} \nabla_\theta \tilde{u}_E.$$

The CAN property (2.15) also implies $\nabla_{\mathcal{M}} u = \nabla u$. Denote $\mathbf{v}_{\mathcal{M}} = \mathbf{B}_2 [\hat{\mathbf{v}}_{\mathcal{M}}]_{\mathbf{B}_2}$ with $[\hat{\mathbf{v}}_{\mathcal{M}}]_{\mathbf{B}_2} = [\|\mathbf{v}_{\mathcal{M}}\|, 0, 0]^T$, where the frame \mathbf{B}_3 is overlapping with \mathbf{B}_2 while $r = 0$. Then, using the definition (2.14), the advection term $\mathbf{v}_{\mathcal{M}}(\mathbf{p}, t) \cdot \nabla_{\mathcal{M}} u(\mathbf{p}, t)$ of the surface PDE (1.1) can be evaluated as

$$(2.24) \quad \mathbf{v}_{\mathcal{M}}(\mathbf{p}, t) \cdot \nabla_{\mathcal{M}} u(\mathbf{p}, t) = [\hat{\mathbf{v}}_{\mathcal{M}}^T]_{\mathbf{B}_2} \nabla_\theta \tilde{u}((\theta_1, \theta_2), t).$$

As mentioned in Remark 2.1, by using the CAN property (2.20) and (2.13), the advection term in the embedded PDE (2.16) can also be transformed into the proposed advection-aligned orthogonal frame, i.e. $\mathbf{B}_3 : (\partial_{\theta_1} X, \partial_{\theta_2} X, \partial_{\theta_3} X) \rightarrow \mathbf{B}_2 : (\hat{\mathbf{T}}_1, \hat{\mathbf{T}}_2, \hat{\mathbf{N}})$,

$$\mathbf{v}_E(\mathbf{x}, t) \cdot \nabla u_E(\mathbf{x}, t) = [\hat{\mathbf{v}}_E^T]_{\mathbf{B}_2} \mathbf{R}^{-1} \nabla_\theta \tilde{u}((\theta_1, \theta_2), t),$$

with the velocity defined in different basis $\mathbf{v}_E = \mathbf{B}_3 [\tilde{\mathbf{v}}_E]_{\mathbf{B}_3} = \mathbf{B}_2 [\hat{\mathbf{v}}_E]_{\mathbf{B}_2}$. Then, under the same orthogonal frame, we can match the coefficients of $\nabla_\theta u$ to get $[\hat{\mathbf{v}}_E^T]_{\mathbf{B}_2} \mathbf{R}^{-1} = [\hat{\mathbf{v}}_{\mathcal{M}}^T]_{\mathbf{B}_2}$. We can finally get $[\hat{\mathbf{v}}]_{\mathbf{B}_2} = \mathbf{R} [\hat{\mathbf{v}}_{\mathcal{M}}]_{\mathbf{B}_2}$ in our constructed frame, which is equivalent to the relation (2.17) by multiplying matrix \mathbf{B}_2 .

Regarding the diffusion term, we have already derived $\nabla \cdot (\mathbf{A}(\mathbf{x}, t) \nabla u_E(\mathbf{x}, t))$ in the embedded domain as (2.19) in Lemma 2.2. Similarly, with the CAN property (2.15), the diffusion term $\Delta_{\mathcal{M}} u(\mathbf{p}, t)$ of the surface PDE (1.1) on \mathcal{M} can be derived as

$$(2.25) \quad \Delta_{\mathcal{M}} u = \nabla \cdot (\tilde{\mathbf{I}} \nabla u) = \text{Tr} \left(\mathbf{B}_2 (\nabla_\theta \nabla_\theta^T) \tilde{u} \mathbf{B}_2^T \tilde{\mathbf{I}} \right),$$

where the surface diffusion tensor is $\tilde{\mathbf{I}} = [1, 0, 0; 0, 1, 0; 0, 0, \tilde{a}]$ with any variable \tilde{a} . For further details on the properties and derivation of $\tilde{\mathbf{I}}$, please refer to [21]. Note that the diffusion term (2.19) of the embedded PDE (2.16) remains in the frame \mathbf{B}_3 . We must apply the CAN property and (2.20) to transform it into the same advection-aligned frame as the diffusion term (2.25) of the surface PDE (1.1). Denote the diffusion tensor $\mathbf{A}(\mathbf{x}, t) = \mathbf{B}_3 \mathbf{A}_X \mathbf{B}_3^{-1} = \mathbf{B}_2 \hat{\mathbf{A}} \mathbf{B}_2^{-1}$ and use (2.12), (2.13) to get

$$\begin{aligned} \nabla \cdot (\mathbf{A} \nabla u_E) &= \nabla_\theta^T \left(\mathbf{B}_2 \hat{\mathbf{A}} \mathbf{B}_2^T \right) \mathbf{R}^{-1} \mathbf{R}^{-T} \nabla_\theta \tilde{u} \\ &\quad + \text{Tr} \left(\mathbf{B}_2^{-T} \mathbf{R}^{-T} (\nabla_\theta \nabla_\theta^T) \tilde{u} \mathbf{R}^{-1} \mathbf{B}_2^{-1} (\mathbf{B}_2 \hat{\mathbf{A}} \mathbf{B}_2^T) \right). \end{aligned}$$

Since all the diffusion terms are both in the advection-aligned frame, we have

$$(2.26) \quad \text{Tr} \left(\mathbf{B}_2^{-T} \mathbf{R}^{-T} (\nabla_\theta \nabla_\theta^T) \tilde{u} \mathbf{R}^{-1} \mathbf{B}_2^{-1} (\mathbf{B}_2 \hat{\mathbf{A}} \mathbf{B}_2^T) \right) = \text{Tr} \left(\mathbf{B}_2 (\nabla_\theta \nabla_\theta^T) \tilde{u} \mathbf{B}_2^T \tilde{\mathbf{I}} \right),$$

$$(2.27) \quad \nabla_\theta^T \left(\mathbf{B}_2 \hat{\mathbf{A}} \mathbf{B}_2^T \right) \mathbf{R}^{-1} \mathbf{R}^{-T} \nabla_\theta \tilde{u} = 0.$$

By applying the CAN properties (2.20)-(2.21), we conclude that the last row and column of the Hessian matrix $(\nabla_\theta \nabla_\theta^T) \tilde{u}$ vanish. Since all the matrices in the derivation

are symmetric and the last row (or equivalently, the last column) of \mathbf{R} is $[0, 0, 1]$, straightforward matrix operations for (2.26) yield the components a_{ij} ($i, j = 1, 2$) of the diffusion tensor \mathbf{A} as $a_{ij} = (\mathbf{B}_2 \hat{\mathbf{A}} \mathbf{B}_2^T)_{ij} = (\mathbf{B}_2 \tilde{\mathbf{I}} \mathbf{B}_2^T)_{ij} = (\mathbf{G}_X)_{ij}$. Note that equation (2.27) corresponds to the first-order differential of \tilde{u} , i.e. $\nabla_\theta \tilde{u}$. Setting this term to zero ensures that the diffusion term does not interfere with the advection term. Based on the equation (2.20), we can match the coefficients with $\nabla_\theta^T (\mathbf{B}_2 \hat{\mathbf{A}} \mathbf{B}_2^T) = [0, 0, \tilde{a}] \mathbf{R} \mathbf{R}^T = [0, 0, \tilde{a}]$. With the components a_{ij} ($i, j = 1, 2, 3$) of $\mathbf{A} = \mathbf{B}_2 \hat{\mathbf{A}} \mathbf{B}_2^T$, a simple algebraic examination shows that

$$(2.28) \quad \partial_{\theta_3} a_{3i} = -\partial_{\theta_1} a_{1i} - \partial_{\theta_2} a_{2i} \quad i = 1, 2,$$

and a_{33} depends solely on \tilde{a} , which means a_{33} can be selected arbitrarily. Note that the equation (2.28) also holds at $r = 0$ with $\mathbf{A} = \tilde{\mathbf{I}}$, thereby providing initial conditions

$$(2.29) \quad a_{3i}(\theta_3 = 0) = 0 \quad i = 1, 2.$$

The equation (2.28) combined with initial conditions (2.29) can become an ODE system for a_{31} and a_{32} with respect to variable θ_3 , with the solution

$$(2.30) \quad a_{3i} = \int_0^r (-\partial_{\theta_1} a_{1i} - \partial_{\theta_2} a_{2i}) \quad i = 1, 2.$$

Finally, one verifies that on the manifold \mathcal{M} , when $r = 0$, the embedded solution recovers the surface quantities

$$(2.31) \quad \mathbf{v}_E(\mathbf{p}, t) = \mathbf{v}_M(\mathbf{p}, t), \quad \mathbf{A}(\mathbf{p}, t) = \tilde{\mathbf{I}}, \quad \forall \mathbf{p} \in \mathcal{M}, t \in [0, T], \quad \text{for } r = 0.$$

For a complete discussion of the embedding condition in the third equation of (2.16), we refer the readers to [22]. \square

3. The Trajectory-Based Method. In the previous section, we embedded the advection-diffusion equation (1.1), defined on the manifold \mathcal{M} , into a narrow band region Ω (2.6) and derived an embedded PDE (2.16) with push-forward operators (2.17)-(2.18). Building on our proposed framework for demonstrating equivalence, as illustrated in Figure 1, we now seek to further decompose the embedded PDE into an operator-split characteristic (OSC) system in Ω through a trajectory-based method. This formulation encompasses an ODE governing the characteristic curves and a diffusion PDE. In this section, we demonstrate the equivalence between the embedded PDE (2.16) and an OSC system to be defined in (3.5) below in the narrow band domain. This OSC system (3.5) can ultimately be restricted back to the manifold \mathcal{M} , resulting in the OSC system on \mathcal{M} , which shows that the original surface advection-diffusion equation (1.1) and the OSC surface system (3.6) are equivalent.

It is important to note that previous works, such as [17] and [18], have established the equivalence between these characteristic methods and the original domain PDE under certain assumptions. Specifically, [17, Prop. 1] showed that, provided the advection velocity is sufficiently regular and vanishes on the boundary of the domain, the characteristic ODE governing the trajectories is well-defined in the discrete setting. Building on this, [18, Prop. 3.1] demonstrated the differentiability of the trajectory mapping, thereby rigorously completing the equivalence argument. However, as derived in the embedded PDE (2.16) in Section 2, it is evident that our push-forward velocity field \mathbf{v}_E (2.17) is not zero at the boundary of the narrow band domain. We can only conclude that the normal component of the velocity is zero because \mathbf{v}_E is

tangential. This distinction necessitates a careful extension of the existing analysis to our setting (see the proof of Lemma 3.1).

We adopt the same notation for characteristic curves \mathcal{X} as in [18, 23]. For given $(\mathbf{x}, t) \in \Omega \times [0, T]$, the characteristic curve based on the trajectory through (\mathbf{x}, t) is the vector function $\mathcal{X}(\cdot; \mathbf{x}, t)$ solving the initial value problem

$$(3.1) \quad \frac{\partial \mathcal{X}}{\partial \tau}(\tau; \mathbf{x}, t) = \mathbf{v}_E(\mathcal{X}(\tau; \mathbf{x}, t), \tau), \quad \text{with initial condition (IC)} : \mathcal{X}(t; \mathbf{x}, t) = \mathbf{x},$$

which simply specifies that for a fixed initial pair (\mathbf{x}, t) , when the tracking time τ equals t , the characteristic curve starts at the point \mathbf{x} . Such initial value problem (3.1) depicts the trajectory of a material point, initially at position \mathbf{x} and time t , as it moves under the influence of the velocity field \mathbf{v}_E to its position \mathcal{X} at time τ . In this case, as a function on $(\tau; \mathbf{x}, t)$, it is Lipschitz continuous in $[0, T] \times \Omega \times [0, T]$, with regularity in \mathbf{x} for fixed t, τ .

It is well-established that the closest point mapping $\text{cp}(\mathbf{x})$ mapping is C^k -smooth for any point \mathbf{x} within the narrow band space for any C^{k+1} -smooth surface [24]. The advection-aligned orthonormal frame constructed in Section 2 ensures that, for each $\mathbf{x} \in \Omega$, the corresponding frame $(\hat{\mathbf{T}}_1, \hat{\mathbf{T}}_2, \hat{\mathbf{N}})(\mathbf{x})$ is well-defined. Based on the expression of push-forward velocity (2.17) from Theorem 2.1 and the regularity assumption (1.2) for the tangential velocity field \mathbf{v}_M , we obtain the following regularity result for the push-forward velocity \mathbf{v}_E

$$(3.2) \quad \begin{cases} \mathbf{v}_E \in C^0([0, T]; C^k(\Omega)), \\ \mathbf{v}_E(\mathbf{x}, t) \cdot \hat{\mathbf{N}}(\mathbf{x}, t) = 0 \quad \forall \mathbf{x} \in \Omega, t \in [0, T]. \end{cases}$$

Drawing inspiration from [17, Prop 1] and [18, Lemma 1], we present the following lemma with different velocity properties to demonstrate the effectiveness of trajectory-based methods in Ω . This indicates that solving equation (3.1) is well-defined across the entire domain Ω and yields a unique solution for each initial condition \mathbf{x} .

LEMMA 3.1. *Under the property (3.2), for any initial point $\mathbf{x} \in \Omega$ at time t and any time $\tau_1, \tau_2 \in (0, T]$, the uniqueness result of (3.1) gives in particular that*

$$(3.3) \quad \mathcal{X}(\tau_2; \mathbf{x}, t) = \mathcal{X}(\tau_2; \mathcal{X}(\tau_1; \mathbf{x}, t), \tau_1) \in \Omega.$$

Indeed, by assuming $\tau_2 = t$, we deduce that the mapping $\mathcal{X}(\tau_2; \cdot, t) : \Omega \rightarrow \Omega$ is one-to-one, with inverse $\mathcal{X}(t; \cdot, \tau_2)$.

Proof. For any initial point $\mathbf{x} \in \Omega$, including those on the boundary $\partial\Omega$, we can always consider that such a point lies within a parallel surface \mathcal{M}_{r_c} (2.9). There exists a smooth function $F : \Omega \rightarrow \mathbb{R}$ such that the parallel surface \mathcal{M}_{r_c} is characterized by

$$\mathcal{M}_{r_c} = \{\mathbf{x} \in \Omega : F(\mathbf{x}) = 0\}.$$

In practice, one often chooses F to be the signed distance function to a reference manifold, so that ∇F is well-defined and satisfies $\|\nabla F(\mathbf{x})\| = 1$ in Ω . Consider the time derivative of F along the characteristic curve $\mathcal{X}(\tau; \mathbf{x}, t)$ defined in (3.1)

$$\frac{\partial}{\partial \tau} F(\mathcal{X}(\tau; \mathbf{x}, t)) = \nabla_{\mathcal{X}} F(\mathcal{X}(\mathbf{x}, t; \tau)) \cdot \frac{\partial \mathcal{X}}{\partial \tau}(\tau; \mathbf{x}, t) = \nabla_{\mathcal{X}} F(\mathcal{X}(\tau; \mathbf{x}, t)) \cdot \mathbf{v}_E(\mathcal{X}(\tau; \mathbf{x}, t), \tau),$$

where the operator $\nabla_{\mathcal{X}}$ denotes the gradient operator for the variable \mathcal{X} . Assume that the path $\mathcal{X}(\tau; \mathbf{x}, t)$ is not exactly on the zero level set \mathcal{M}_r , it can lie on some

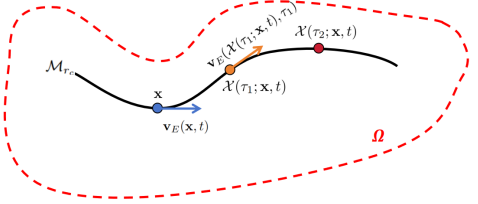


Fig. 3: Schematic illustration of the characteristic curve $\mathcal{X}(\tau; \mathbf{x}, t)$ evolving within the narrow band domain Ω (bounded by a red dashed outline). The initial point \mathbf{x} (blue dot) lies on the parallel surface \mathcal{M}_{r_c} (depicted as a continuous black curve). Under the tangential velocity \mathbf{v}_E , \mathbf{x} is carried first to $\mathcal{X}(\tau_1; \mathbf{x}, t)$ (orange dot) and then further to $\mathcal{X}(\tau_2; \mathcal{X}(\tau_1; \mathbf{x}, t), \tau_1)$ (red dot). This two-stage progression is equivalent to directly moving from \mathbf{x} to $\mathcal{X}(\tau_2; \mathbf{x}, t)$.

other level set of F . At that point \mathcal{X} , $\nabla_{\mathcal{X}} F(\mathcal{X}(\tau; \mathbf{x}, t))$ is the unit normal to the parallel surface (the level set of F) that passes through $\mathcal{X}(\tau; \mathbf{x}, t)$. Hence, we still have $\mathbf{v}_E \cdot \nabla_{\mathcal{X}} F = 0$ at $\mathcal{X}(\tau; \mathbf{x}, t)$ for all $\tau \in [0, T]$. Since the derivative simplifies to zero, the value of F is constant along the trajectory. The initial condition in (3.1) gives $F(\mathcal{X}(\tau; \mathbf{x}, t)) = F(\mathcal{X}(t; \mathbf{x}, t)) = 0$ for all $\tau \in [0, T]$. This shows that \mathcal{X} remains on $\mathcal{M}_r \subset \Omega$ for all $\tau \in [0, T]$ (Figure 3 provides a simple geometric explanation). By the uniqueness theory of ODE [25], the solution of (3.1) ensures that $\mathcal{X}(\tau_2; \mathbf{x}, t) = \mathcal{X}(\tau_2; \mathcal{X}(\tau_1; \mathbf{x}, t), \tau_1)$ for any $\tau_1, \tau_2 \in [0, T]$, when guarantees a one-to-one mapping. \square

Next, based on Lemma 3.1, we refer to [18, Prop 3.1] to ensure that the flow map $\mathcal{X}(\tau; \mathbf{x}, t)$ is sufficiently smooth in \mathbf{x} , so that first and second spatial derivatives exist. Then, using the chain rule and equation (3.1), we have

$$\begin{aligned}
 \frac{d}{d\tau} u_E(\mathcal{X}(\tau; \mathbf{x}, t), \tau) &= \frac{\partial u_E(\mathcal{X}(\tau; \mathbf{x}, t), \tau)}{\partial t} + \sum_{j=1}^d \frac{\partial u_E(\mathcal{X}(\tau; \mathbf{x}, t), \tau)}{\partial \mathbf{x}_j} \frac{\partial \mathcal{X}_j}{\partial \tau} \\
 (3.4) \quad &= \frac{\partial}{\partial t} u_E(\mathcal{X}(\tau; \mathbf{x}, t), \tau) + \mathbf{v}_E \cdot \nabla u_E(\mathcal{X}(\tau; \mathbf{x}, t), \tau),
 \end{aligned}$$

which is referred to as the total (material) derivative of u_E with respect to $\tau \in [0, T]$ (same formulation as [23, (12.5.4)]). By writing (2.16) at point $\mathcal{X}(\tau; \mathbf{x}, t)$ and time τ , and using (3.4), we have the following operator-split characteristic (OSC) system

$$\begin{cases}
 \frac{\partial}{\partial \tau} \mathcal{X}(\tau; \mathbf{x}, t) = \mathbf{v}_E(\mathcal{X}(\tau; \mathbf{x}, t), \tau), & \text{with IC : } \mathcal{X}(t; \mathbf{x}, t) = \mathbf{x}, \\
 \frac{du_E}{d\tau}(\mathcal{X}, \tau) = \varepsilon \nabla \cdot (\mathbf{A}(\mathcal{X}) \nabla u_E(\mathcal{X}, \tau)) & \text{in } \Omega, \tau \in [0, T], \\
 u_E(\cdot, 0) = u(\text{cp}(\cdot), 0) & \text{in } \Omega, \\
 \partial_{\mathbf{N}} u_E(\mathcal{X}, \tau) = 0 \quad \text{and} \quad \partial_{\mathbf{N}}^{(2)} u_E(\mathcal{X}, \tau) = 0, & \text{on } \mathcal{M}, \tau \in [0, T].
 \end{cases} \quad (3.5)$$

Building on the proof of Lemma 3.1, the characteristic curves \mathcal{X} are parallel with the manifold \mathcal{M} , which implies $\text{cp}(\mathcal{X}(\tau; \mathbf{x}, t)) = \mathcal{X}(\tau; \mathbf{p}, t)$. By restricting $\mathcal{X}(\tau; \mathbf{x}, t)$ to the manifold \mathcal{M} and employing the definitions of push-forward velocity and diffusion tensor (2.17)-(2.18), we can directly derive the OSC system on \mathcal{M} by trajectory-based

method as follows

$$(3.6) \quad \begin{cases} \frac{\partial \mathcal{X}}{\partial \tau}(\tau; \mathbf{p}, t) = \mathbf{v}_{\mathcal{M}}(\mathcal{X}(\tau; \mathbf{p}, t), \tau), & \text{with IC : } \mathcal{X}(t; \mathbf{p}, t) = \mathbf{p} \in \mathcal{M}, \\ \frac{du}{d\tau}(\mathcal{X}(\tau; \mathbf{p}, t), \tau) = \varepsilon \Delta_{\mathcal{M}} u(\mathcal{X}(\tau; \mathbf{p}, t), \tau) & \text{on } \mathcal{M}, \tau \in [0, T]. \end{cases}$$

It is important to note that the validity of the above derivation relies on the embedded PDE with the push-forward operators preserving the CAN property of time continuity.

In summary, we have successfully established the equivalence framework illustrated in Figure 1, rigorously demonstrating the equivalence between the original surface advection-diffusion equation (1.1) and the OSC surface system (3.6) on the manifold \mathcal{M} . The OSC system (3.6) splits the surface advection-diffusion problem (1.1) into two independent stages: tracking the characteristic curves generated by the tangential velocity field, and solving a purely diffusive equation along those trajectories. Because the advection part is treated exactly by the flow map, the remaining diffusion step can be discretised with any convenient spatial scheme—finite differences, finite elements, or mesh-free radial basis functions. Herein, we focus on the Kansa-type RBF collocation algorithm specifically adapted to the OSC system (3.6).

4. Kansa-Type RBF Collocation Algorithm for OSC System. Based on the rigorous derivation presented above, we have established that the advection-diffusion equation (1.1) on \mathcal{M} is equivalent to the trajectory-based PDEs (3.6). In this section, we develop efficient numerical algorithms for such trajectory-based PDEs.

The trajectory-based method often requires determining the departure point for a given spatial location at a later time. This is accomplished by backtracing the characteristic line from any point $\mathbf{p} \in \mathcal{M}$ at time t_{n+1} to its origin at time t_n . Referring to [15], we also employ an s -stage surface-restricted explicit Runge-Kutta (RK) method to solve the first ODE in (3.6), which is shown as

$$(4.1) \quad \begin{cases} \mathbf{k}_i = \mathbf{v}_{\mathcal{M}} \left(\text{cp} \left(\mathbf{p} - \Delta t \sum_{j=1}^{i-1} a_{ij} \mathbf{k}_j \right), t_{n+1} - c_i \Delta t \right), & i = 1, \dots, s, \\ \mathcal{X}(t_n; \mathbf{p}, t_{n+1}) = \text{cp} \left(\mathbf{p} - \Delta t \sum_{j=1}^s b_j \mathbf{k}_j \right) \in \mathcal{M}, \end{cases}$$

where $\Delta t := t_{n+1} - t_n$, and the coefficients a_{ij}, b_j , and c_i define the RK scheme. It is important to note that we also adopt the closest point mapping in the second equation of (4.1) to ensure that the new approximation point remains on the manifold \mathcal{M} . The convergence of the surface-restricted RK scheme is proved in [15, Thm. 2].

To compute $u(\mathbf{p}, t_{n+1})$ from the second PDE in (3.6), we have many options and introduce the time stepping scheme of the following Crank-Nicolson (CN) scheme

$$\begin{aligned} & \frac{u^{n+1}(\mathcal{X}(\tau_{n+1}; \mathbf{p}, t_{n+1})) - u^n(\mathcal{X}(\tau_n; \mathbf{p}, t_{n+1}))}{\Delta \tau} \\ &= \frac{\varepsilon}{2} (\Delta_{\mathcal{M}} u^{n+1}(\mathcal{X}(\tau_{n+1}; \mathbf{p}, t_{n+1})) + \Delta_{\mathcal{M}} u^n(\mathcal{X}(\tau_n; \mathbf{p}, t_{n+1}))) \end{aligned}$$

Note that $\mathcal{X}(\tau_{n+1}; \mathbf{p}, t_{n+1}) = \mathbf{p}$ with $\tau_n = t_n$ and we only have information about fixed point \mathbf{p} from the previous time step. Hence, we denote $u^n(\mathbf{p})$ as the solution $u(\mathbf{p}, t^n)$ at the point \mathbf{p} for time t^n and $\Pi u^n(\mathcal{X}(t_n; \mathbf{p}, t_{n+1}))$ as the interpolation of the

value of $u^n(\cdot)$. With these definitions, the CN scheme is given by

$$(4.2) \quad \begin{cases} \tilde{u}^n(\mathcal{X}(t_n; \mathbf{p}, t_{n+1})) := \Pi u^n(\mathcal{X}(t_n; \mathbf{p}, t_{n+1})), \\ \frac{u^{n+1}(\mathbf{p}) - \tilde{u}^n(\mathcal{X}(t_n; \mathbf{p}, t_{n+1}))}{\Delta t} = \frac{\varepsilon}{2} (\Delta_{\mathcal{M}} u^{n+1}(\mathbf{p}) + \Delta_{\mathcal{M}} \tilde{u}^n(\mathcal{X}(t_n; \mathbf{p}, t_{n+1}))). \end{cases}$$

Other time stepping methods, such as the BDF scheme, can be defined similarly. For instance, we also tested BDF methods of various time orders in our experiments, though these results are not detailed here. Note that equation (4.2) contains a term $\Delta_{\mathcal{M}} \tilde{u}^n(\mathcal{X}(t_n; \mathbf{p}, t_{n+1}))$, which requires the utilization of information from surrounding points during the spatial discretization process. However, the finite difference and finite element methods face significant challenges in acquiring data on backtracked points, given that only data from specified points are available. In the case of RBF closest point method, as proposed in [16], backtracking interpolation requires information from surrounding points, which must leverage the CAN property. Hence, each time step needs to be interpolated back to the surface or employ the embedded PDE (2.16) derived in Section 2 for the calculation. To effectively tackle these challenges and circumvent issues related to CAN property, we implement the Kansa-type RBF collocation method for spatial discretization.

We employ symmetric positive definite (SPD) radial basis functions (RBFs) $\Phi_m : \mathbb{R}^d \times \mathbb{R}^d \rightarrow \mathbb{R}$ that are shift-invariant and radial in nature. Following the framework established in [26], we use kernel functions of the form $\Phi_m(\|\mathbf{p} - \mathbf{z}\|)$ whose Fourier transforms exhibit algebraic decay properties.

Let the sets of quasi-uniform trial centers be $Z = \{\mathbf{z}_1, \dots, \mathbf{z}_{n_Z}\} \subset \mathcal{M}$, and collocation points be $P = \{\mathbf{p}_1, \dots, \mathbf{p}_{n_p}\} \subset \mathcal{M}$. The fill distance h on \mathcal{M} with respect to Z is defined as $h = h_Z := \sup_{\xi \in \mathcal{M}} \min_{\mathbf{z}_j \in Z} \|\xi - \mathbf{z}_j\|_{\ell^2(\mathbb{R}^d)}$. Given a set of trials Z and the kernel Φ_m , the finite-dimensional trial space \mathcal{U}_Z is defined as $\mathcal{U}_Z := \text{span}\{\Phi_m(\cdot, \mathbf{z}_j) \mid \mathbf{z}_j \in Z\}$, with the fully discrete solution $u_Z^n(\cdot) = \sum_{j=1}^{n_Z} \lambda_j^n \Phi_m(\cdot, \mathbf{z}_j) = \Phi_m(\cdot, Z) \boldsymbol{\lambda}^n$, for $n \geq 0$. We define the closest point at time t_n traced back along the characteristic line from the collocation points P at time t_{n+1} as $\mathcal{X}_n := \mathcal{X}(t_n; P, t_{n+1})$. By substituting \mathcal{X}_n and $u_Z^n(\cdot)$ into the CN scheme (4.2) and the initial condition $\boldsymbol{\lambda}^0 = \Phi_m(P, Z)^{-1} u_{\mathcal{M}, 0}(P)$ ($\Phi_m(P, Z)$ is the collocation matrix), we obtain

$$(4.3) \quad \begin{aligned} \left(\Phi_m(P, Z) - \frac{\varepsilon}{2} \Delta t \Delta_{\mathcal{M}} \Phi_m(P, Z) \right) \boldsymbol{\lambda}^{n+1} \\ = \left(\Phi_m(\mathcal{X}_{n-1}, Z) + \frac{\varepsilon}{2} \Delta t \Delta_{\mathcal{M}} \Phi_m(\mathcal{X}_{n-1}, Z) \right) \boldsymbol{\lambda}^n. \end{aligned}$$

which already incorporates the handling of the interpolation mapping Π . The extrinsic formula of the Laplace-Beltrami operator $\Delta_{\mathcal{M}}$ can be referred to [27, Eq. (4.2)].

The trajectory-based advection-diffusion equations (3.6) are fully discretized utilizing CN time discretization, in conjunction with Kansa-type RBF collocation spatial discretization. Below, we summarize the numerical framework of the Trajectory Based RBF Collocation (TBRBF) algorithm as following Alg. 1.

5. Numerical Experiments. In this section, we conduct numerical experiments to assess the performance of the proposed TBRBF method in solving surface advection-diffusion equations on compact, smooth manifolds. The TBRBF method is first tested on the unit circle, showcasing optimal error convergence in time and superconvergence in space. Subsequently, the algorithm is evaluated using initial conditions with singularities on both the unit circle and the torus, demonstrating that the proposed method offers enhanced stability compared to the traditional Kansa

Algorithm 1: Trajectory Based RBF Collocation (TBRBF) Algorithm

Step 1: Identify the backtraced points: For each surface point $\mathbf{p}_i \in P$, solve the first ODE in (3.6) over the time interval $[t_n, t_{n+1}]$ by the surface-restricted RK (4.1) to identify the backtraced points $\mathcal{X}_n := \mathcal{X}(t_n; P, t_{n+1})$ for $j = 1, \dots, k$.

Step 2: Interpolate the solution on the backtraced points: Use existing nodal solution values $\{P, u_Z^n(P)\}$ as data and RBF discretization $u_Z^n(\cdot)$ to interpolate the solution $\{\bar{u}_Z^n\}$ in the backtraced points $\{\mathcal{X}_n\}$, then use $u_Z^n(\cdot)$ to get λ^{n-j+1} .

Step 3: Solve the PDE to update the nodal solution: Solve the fully discretization formulation (4.3) over the time interval $[t_n, t_{n+1}]$ to get λ^{n+1} , then recall RBF discretization $u_Z^n(\cdot)$ to obtain the next time level solution $u_Z^{n+1}(P)$. Other numerical discretization schemes can also be applied.

method. Next, we investigate the two-species Turing system with advection terms, which serves as a benchmark problem for testing numerical methods for surface PDEs. This helps to further highlight the capabilities of our TBRBF method. Finally, we extend the Turing pattern simulation to complex point clouds, providing additional evidence of the algorithm's effectiveness and wide-ranging applicability.

In all numerical tests, we use the standard Whittle-Matérn Sobolev kernel [28] to develop the kernel required for our RBF formulation, which is shown as

$$\Phi_m(\mathbf{p}, \mathbf{z}) := \frac{2^{1-m+\frac{d}{2}}}{(m - \frac{d}{2})!} \|\mathbf{p} - \mathbf{z}\|_{\ell^2}^{m-\frac{d}{2}} \mathcal{K}_{m-\frac{d}{2}}(\|\mathbf{p} - \mathbf{z}\|_{\ell^2}) \quad \forall \mathbf{p}, \mathbf{z} \in \mathcal{M},$$

where \mathcal{K}_ν is the modified Bessel function of the second kind of order ν . Furthermore, we assume that the collection points are always the same as the trial centers in our simulations. For all the implicit surfaces discussed later, including the torus, sphere, Bretzel2 and CPD surfaces, we present their implicit expressions along with the corresponding tangential advection velocities in Appendix A. Furthermore, we have used a modified version of the *distmeshsurface* algorithm [29] to obtain trial centers or collection points on various surfaces. The source code is implemented in MATLAB and can be found in the repository [30].

5.1. Example 1: Convergence tests on the circle. In this subsection, we analyze the convergence of our numerical method for approximating the advection-diffusion equation in (1.1) with the advection velocity field $\mathbf{v}(\theta) = [-\sin(\theta), \cos(\theta)]^T$. For the convergence test, we select the exact solution $u^*(\theta, t) = \exp(-\varepsilon t) \cos(\theta - t)$ from which the initial conditions can be directly obtained.

We employ the surface-restricted RK method (4.1) with various orders $s = 1, 2, 3$ to handle backtracking points and integrate them with the CN (4.2) or BDF scheme of matching time orders for temporal discretization for the PDE of (3.5). Then, we use Matérn kernel with different orders m in (4.3) for spatial discretization to investigate the spatial and temporal convergence of the proposed TBRBF method. In addition, we evaluate the impact of the diffusion coefficient ε by examining some different values, a larger value ($\varepsilon = 1$) to a much smaller value ($\varepsilon = 1e-5$).

To assess the temporal convergence of the TBRBF method, we set the number of collection points $n_P = 200$, resulting in a spatial step size (fill distance) of $h = \frac{2\pi}{n_P}$. And we fix the kernel smoothness order at $m = 5$. We then select various time steps $\Delta t = 0.1, 0.05, 0.01, 0.001$ and evolve the solutions until a final time of $T = 1.0$. The

absolute error of the ℓ^∞ norm is used to compare the numerical solution with the exact one. As illustrated in Table 1, TBRBF achieves the expected convergence order under the RK2-CN scheme.

Table 1: **(Example 1)** The temporal convergence of the RK2-CN shceme for different ε when solving (1.1) on the unit circle ($h = \frac{2\pi}{200}$, $m = 5$, and $T = 1.0$).

Δt	$\varepsilon = 1$		$\varepsilon = 1e - 3$		$\varepsilon = 1e - 5$	
	ℓ^∞ error	rate	ℓ^∞ error	rate	ℓ^∞ error	rate
0.10	8.38e-04	—	3.73e-04	—	3.73e-04	—
0.05	2.21e-04	1.92	9.88e-05	1.92	9.88e-05	1.92
0.01	9.22e-06	1.98	4.12e-06	1.98	4.12e-06	1.98
0.001	9.31e-08	2.00	4.16e-08	2.00	4.16e-08	2.00

For the spatial convergence of TBRBF, we adopt a small time step of $\Delta t = 10^{-4}$ and a total time of $T = 1.0$, ensuring that the observed errors are dominated by spatial discretization. Using the BDF3 time-stepping scheme, we investigate the effects of various fill distances h and kernel smoothness orders m . The results, summarized in Table 2, demonstrate that spatial discretization achieves superconvergent behavior.

Table 2: **(Example 1)** The spatial convergence of TBRBF for different ε and kernel smoothness orders ($m = 3, 4, 5$) when solving (1.1) on the unit circle at $T = 1.0$ with small time step $\Delta t = 10^{-4}$ using the BDF3 with RK3.

ε	h	$m = 3$		$m = 4$		$m = 5$	
		ℓ^∞ error	rate	ℓ^∞ error	rate	ℓ^∞ error	rate
1	$\frac{2\pi}{50}$	2.88e-01	—	5.85e-03	—	1.15e-04	—
	$\frac{2\pi}{80}$	8.16e-02	2.79	5.80e-04	4.94	4.47e-06	6.93
	$\frac{2\pi}{100}$	4.29e-02	2.88	1.91e-04	4.96	9.46e-07	6.96
	$\frac{2\pi}{120}$	2.51e-02	2.93	7.73e-05	4.98	2.65e-07	6.97
$1e - 5$	$\frac{2\pi}{50}$	5.73e-04	—	1.56e-05	—	4.03e-07	—
	$\frac{2\pi}{80}$	5.68e-05	4.94	6.12e-07	6.93	6.19e-09	8.92
	$\frac{2\pi}{100}$	1.88e-05	4.96	1.30e-07	6.95	8.45e-10	8.93
	$\frac{2\pi}{120}$	7.59e-06	4.97	3.64e-08	6.97	1.67e-10	8.90

5.2. Example 2: Modified Shu's linear test with non-smooth initial data. In this example, we employ a modified version of Shu's linear test [31], namely a non-smooth multi-wave initial condition, to further evaluate the stability of our method in comparison to the traditional Kansa method on the unit circle. In this modification, the original discontinuous line segments are replaced with corresponding singularity points represented by a piecewise continuous trapezoidal function. As a result, the modified multi-wave initial condition consists of four components: a smooth Gaussian function, a piecewise continuous trapezoidal function, a piecewise

continuous triangular function, and a smooth elliptical function

$$u_0(\theta) = \begin{cases} \frac{1}{6}G(\theta/\pi, \alpha, z + \delta) + \frac{4}{6}G(\theta/\pi, \alpha, z) + \frac{1}{6}G(\theta/\pi, \alpha, z - \delta), & \theta \in [\frac{1}{5}\pi, \frac{2}{5}\pi], \\ 20\theta - 35, & \theta \in [1.75, 1.8], \\ 1, & \theta \in [1.8, 2.5], \\ -20\theta + 51, & \theta \in [2.5, 2.65], \\ 1 - |2.5\theta - 8.5|, & \theta \in [3, 3.8], \\ \frac{1}{6}F(\theta/\pi, \beta, b + \delta) + \frac{4}{6}F(\theta/\pi, \beta, b) + \frac{1}{6}F(\theta/\pi, \beta, b - \delta), & \theta \in [\frac{7}{5}\pi, \frac{8}{5}\pi], \\ 0, & \text{otherwise.} \end{cases}$$

where

$$G(\theta, \alpha, z) = e^{-\alpha(\theta-z)^2}, \quad F(\theta, \beta, b) = \sqrt{\max(1 - \beta^2(\theta-b)^2, 0)},$$

with $\alpha = \log 2/(36\delta^2)$, $\beta = 10$, $z = 0.3$, $b = 1.5$, and $\delta = 0.005$. For simplicity, we use the same velocity defined in Example 1 $\mathbf{v}(\theta) = [-\sin(\theta), \cos(\theta)]^T$. We then apply the RK2 method in conjunction with the CN scheme for time discretization, while employing the Matérn kernel with a smoothness order of $m = 4$ for spatial discretization. The number of collection points is fixed at $n_P = 500$ and the time step is set to $\Delta t = 0.01$ with a final time of $T = 2\pi$.

We evaluate the accuracy of our TBRBF method compared to the traditional Kansa method on various diffusion coefficients, $\varepsilon \in \{1e-3, 1e-4, 1e-5, 1e-6\}$. As shown in Figure 4, when the diffusion coefficient ε drops below $1e-4$, the final solution displays oscillations, especially near the corners of the trapezoidal region, leading to instability. In contrast, our proposed method yields stable numerical results.

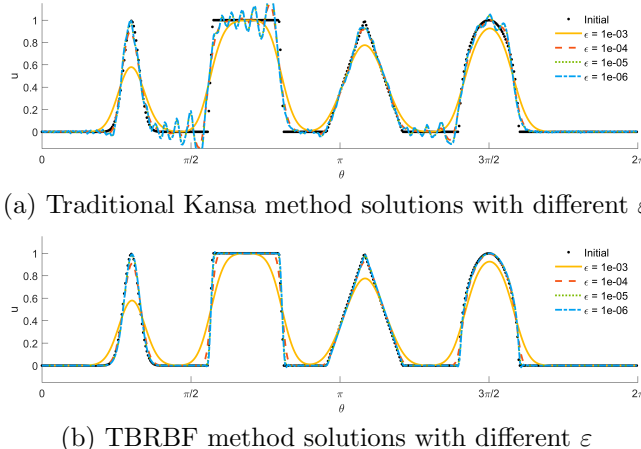


Fig. 4: **(Example 2)** Comparison between traditional Kansa method (top) and TBRBF method (bottom) to solve (1.1) on the unit circle with non-smooth initial data and different diffusion coefficients $\varepsilon \in \{1e-3, 1e-4, 1e-5, 1e-6\}$ (Modified Shu's Linear test with $T = 2\pi$, $\Delta t = 0.01$, $n_P = 500$, $m = 4$).

As is well known, semi-Lagrangian or characteristic methods exhibit unconditional stability, suggesting that the TBRBF method should also remain stable at larger time

steps. For smaller values of diffusion coefficient $\varepsilon = 10^{-6}$, we compared the stability of solutions over different time steps. As illustrated in Figure 5, even with a relatively large time step of $\Delta t = 10^{-2}$, our proposed method demonstrates good stability, while traditional methods require a time step of $\Delta t \leq 10^{-3}$ to maintain stability. This characteristic opens up opportunities for simulating complex geometries in the future, enabling the acquisition of long time solutions while significantly reducing computation time and costs compared to traditional algorithms.

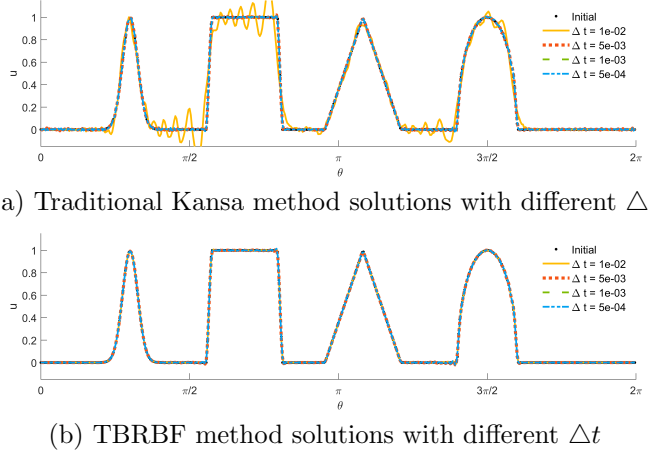


Fig. 5: **(Example 2)** Performance comparison using traditional Kansa method (top) and TBRBF method (bottom) to solve (1.1) on the unit circle with non-smooth initial data and varying time steps $\Delta t \in \{0.01, 0.005, 0.001, 0.0005\}$ (Modified Shu's Linear test with $T = 2\pi$, $n_P = 500$, $\varepsilon = 1e-6$, $m = 4$).

5.3. Example 3: Toroidal dynamics with singularity data on the torus.

We extend the stability analysis from the unit circle to the surface experiment described in [15], where the field $u(x, t)$ evolves under a time-independent velocity field $\mathbf{v} = (v_x, v_y, v_z)$ on a torus with an inner radius of $1/3$ and an outer radius of 1 . Details on the implicit surface representation and velocity expressions are provided in section A. The velocity field specified in section A advects particles along a $(3,2)$ torus knot, returning them to their initial positions after a period $T = 2\pi$.

In this case, as the independent variables of velocity are θ and ϕ , we adopt a parametric representation and specify a singular initial condition

$$(5.1) \quad u(\theta, \phi) = |\sin(2\theta)| + |\cos(2\phi)| - 0.7|\sin(2\theta)\cos(2\phi)|.$$

To aid visualization, Figure 6 presents this initial condition: the left panel shows the condition mapped onto the torus, while the right one provides an intuitive view of the singularity in parameter space.

To emphasize the advection-dominated nature of the surface advection-diffusion equation (1.1), we set the diffusion coefficient to a small value $\varepsilon = 10^{-6}$, which can significantly impact the stability of the numerical solution. We employ an RK2-CN time-stepping scheme (with $T = 2\pi$ and $\Delta t = \frac{\pi}{500}$), while spatial discretization uses $n_P = 11600$ collection points and the Matérn kernel with smoothness order $m = 6$.

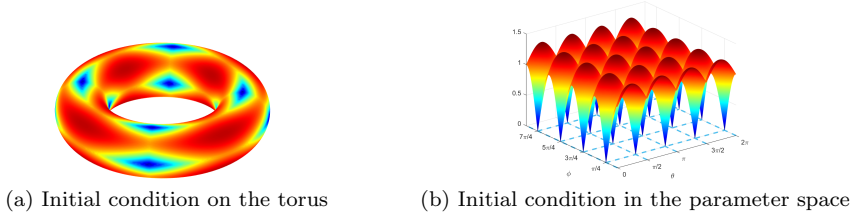


Fig. 6: **(Example 3)** Visualization of the singular initial condition on the torus. Left: The initial condition $u(\theta, \phi)$ displayed on the torus surface. Right: The initial condition represented in the parameter space (θ, ϕ) , clearly highlighting the location and structure of the singularity (blue dashed).

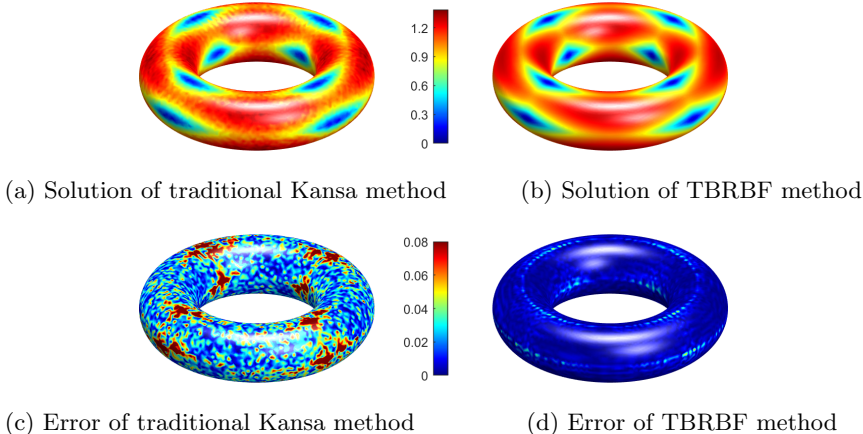


Fig. 7: **(Example 3)** Numerical solutions and corresponding errors for solving (1.1) on a torus with a (3,2) torus knot velocity. The top-left panel shows the solution obtained using the traditional Kansa method, while the top-right panel shows the solution obtained using the TBRBF method. The bottom-left and bottom-right panels display the corresponding errors with respect to the reference solution for the traditional Kansa method and the proposed method, respectively. Discretization parameters used are $(T, \Delta t, n_P, m) = (2\pi, \pi/500, 11600, 6)$.

Given the small value of ε and the fact that $T = 2\pi$ represents a complete rotation, we use the initial condition as a reference solution. As shown in Figure 7, the conventional Kansa method performs poorly, producing significant inaccuracies due to the singularity and the small value of ε . In contrast, our proposed method maintains the integrity of the solution's shape and achieves high accuracy, even with the singular initial condition.

5.4. Example 4: Turing patterns model with advection terms. We now illustrate the effectiveness of the proposed TBRBF method by applying it to reaction–advection–diffusion systems on a variety of general surfaces, which serve as benchmark problems for surface PDEs [10]. Following the numerical experiments in [16], we consider the two-species Turing system with advection velocity \mathbf{v} as defined in section A, posed on the sphere, torus, Bretzel2, and CPD surfaces (each implicitly

defined by algebraic equations in section A)

$$(5.2) \quad \begin{aligned} \partial_t u + \nabla_{\mathcal{M}} \cdot (u \mathbf{v}) &= \varepsilon_u \Delta_{\mathcal{M}} u + au(1 - k_1 w^2) + w(1 - k_2 u), \\ \partial_t w + \nabla_{\mathcal{M}} \cdot (w \mathbf{v}) &= \varepsilon_w \Delta_{\mathcal{M}} w + bw \left(1 + \frac{ak_1}{b} uw \right) + u(c + k_2 w). \end{aligned}$$

The model parameters depend on the specific surface but satisfy the relations $\varepsilon_u = 0.516\varepsilon_w$, $a = -c = 0.899$, and $b = -0.91$. The remaining parameters, including those for the spots and stripes on each surface, are provided in Table 3. The initial condition is generated by assigning uniformly random values in the range $[-0.5, 0.5]$ within a narrow strip along the surface's equator, with zeros elsewhere.

Table 3: **(Example 4)** The parameters of the Turing system used to simulate the spots and stripes with $\varepsilon_u = 0.516\varepsilon_w$, $b = -0.91$, $a = -c = 0.899$.

Surface	Pattern	ε_w	k_1	k_2	Final time
Sphere	Spots	$6.50e-3$	0.02	0.2	600
	Stripes	$8.87e-4$	3.5	0	6000
Torus	Spots	$3.50e-3$	0.02	0.2	1200
	Stripes	$8.87e-4$	3.5	0	6000
Bretzel2	Spots	$2.50e-3$	0.02	0.2	1000
	Stripes	$1.80e-4$	3.5	0	6000
CPD surface	Spots	$2.50e-3$	0.02	0.2	600
	Stripes	$3.50e-4$	3.5	0	8000

We apply the proposed TBRBF method to simulate the Turing patterns model, utilizing the RK2-CN scheme with a time step of $\Delta t = 0.5$ for temporal discretization and the Matérn kernel with smoothness order $m = 4$ for spatial. Since all surfaces under consideration are defined implicitly, the normal vectors $\hat{\mathbf{N}}$ can be calculated exactly. For the closest point computations required by the surface-restricted RK method, we directly use MATLAB's built-in nonlinear optimization solver, configured with the sequential quadratic programming (SQP) algorithm.

The simulation results are presented in Figure 8, where lighter and darker shades indicate higher and lower concentrations, respectively. The first column of Figure 8 visualizes the advection velocity field, allowing observation of the transport dynamics for both the Spots and Stripes systems. As shown in Figure 8, our method successfully generates dynamic Spots that are advected across the surface by the flow. For the Stripes system, while the localized effects of the velocity field on the Bretzel2 and CPD surfaces prevent the development of sharply defined boundaries, the flow nonetheless induces a clear alignment of the patterns along its direction.

5.5. Example 5: Point Clouds Extension for Turing Patterns. To further demonstrate the versatility of our approach, we apply the TBRBF method, using the same discretization schemes and parameter settings as subsection 5.4 Example 4, to more general point cloud surfaces that lack explicit implicit or parametric representations. Specifically, we test on the Stanford Bunny and cow models. The surface reaction–advection–diffusion system (5.2) is used, with model parameters provided in Table 4.

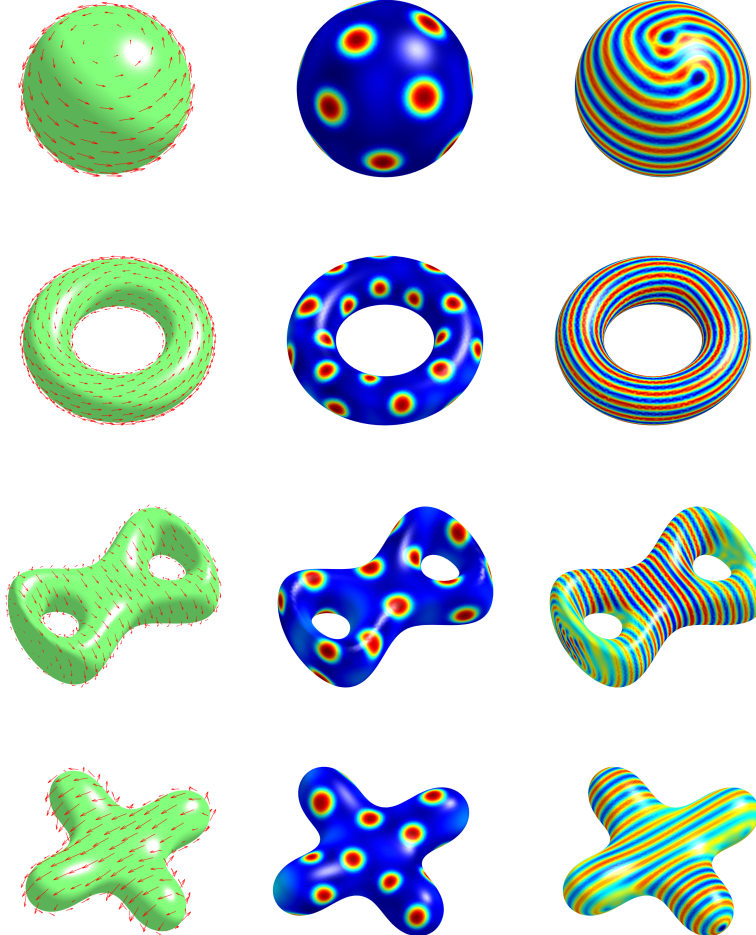


Fig. 8: **(Example 4)** Spots and Stripes on four distinct implicit surfaces: Sphere ($n_P = 4482$), Torus ($n_P = 5312$), Bretzel2 ($n_P = 7216$) and CPD surface ($n_P = 6256$). In each row, the left panel shows the velocity vector field, while the middle and right panels display the spots and stripes, respectively.

Unlike implicit surfaces, exact normal vectors are not directly available for point clouds. Therefore, we estimate the normal vector at each point using localized level-set interpolation. For each point in the cloud, the estimated local normal is first aligned with the z -axis through a suitable rotation, and the local surface is reconstructed using an intrinsic method. The closest point is subsequently refined using Newton's method. Further implementation details can be found in [15].

With these procedures, we obtain the simulation results shown in Figure 9. Similar to the patterns observed in Figure 8, our method successfully captures the characteristic spot and stripe patterns of the Turing system on complex point cloud surfaces. The dynamic evolution and organization of these patterns are well preserved, demonstrating the robustness and adaptability of our approach even in the absence of explicit surface representations.

Table 4: **(Example 5)** The parameters of the Turing system used to simulate the spots and stripes on the Stanford Bunny and Cow with $\varepsilon_u = 0.516\varepsilon_w$, $b = -0.91$, $a = -c = 0.899$.

Surface	Pattern	ε_w	k_1	k_2	Final time
Stanford Bunny & Cow	Spots	$1.50e-3$	0.02	0.2	600
	Stripes	$8.87e-4$	3.0	0	6000

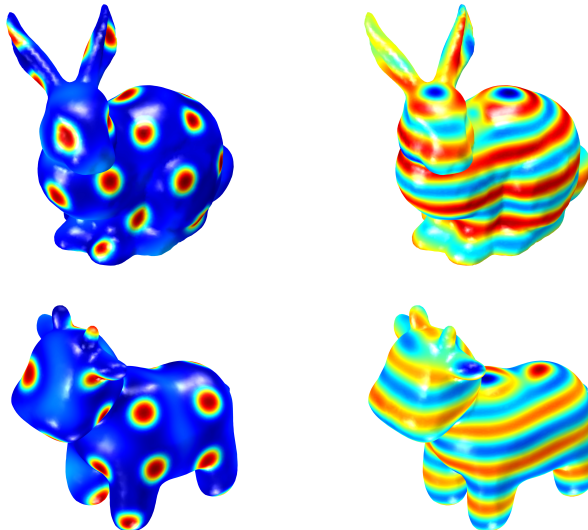


Fig. 9: **(Example 5)** Simulation of Turing patterns on point cloud surfaces using the proposed TBRBF method. Results are shown for Stanford Bunny ($n_P = 15685$) and Cow ($n_P = 14358$).

6. Conclusion. In this paper, we present a TBRBF method for solving the surface advection-diffusion equation on a closed, smooth, compact codimension-1 manifold. By integrating Kansa-type RBF collocation with a trajectory-based framework, our approach directly processes the Laplace–Beltrami operator on the manifold while tracking the evolution of the solution along the advection velocity trajectories. This method effectively avoids the challenges of repeated interpolation in narrow bands, significantly reducing computational complexity. We rigorously established the equivalence between the original surface advection-diffusion PDE and the OSC surface system by embedding the problem into a narrow band. Numerical experiments further validate the enhanced stability and accuracy of our proposed method. Overall, this work provides a robust computational strategy for handling surface PDEs while establishing a solid theoretical foundation for surface trajectory-based formulations.

Additionally, this article offers insights into using time-continuous embedded methods to tackle time-dependent problems, such as heat equations, advection diffusion reaction problems, and Navier-Stokes equations. This approach eliminates the need for repeated use of CAN properties and interpolation methods to return to the manifold closure points. Looking ahead, we aim to extend this method to solve Navier-Stokes equations and thin shell problems. However, it is important to note

that the proposed method currently struggles with shock and oscillation problems, and our future work will focus on addressing these challenges.

Appendix A. Implicit algebraic equations and advecton velocities for all tested manifolds.

The implicit algebraic equations for general surfaces are defined

- Sphere : $\{(x, y) \in \mathbb{R}^2 \mid x^2 + y^2 = 1\}$.
- Torus : $\{(x, y, z) \in \mathbb{R}^3 \mid (x^2 + y^2 + z^2 + 1^2 - (1/3)^2)^2 - 4(x^2 + y^2) = 0\}$.
- Bretzel2 : $\{(x, y, z) \in \mathbb{R}^3 \mid (x^2(1 - x^2) + y^2)^2 + 1/2z^2 - 1/40(x^2 + y^2 + z^2) = 1/40\}$.
- CPD surface : $\{(x, y, z) \in \mathbb{R}^3 \mid \sqrt{(x-1)^2 + y^2 + z^2} \sqrt{(x+1)^2 + y^2 + z^2} \sqrt{x^2 + (y-1)^2 + z^2} \sqrt{x^2 + (y+1)^2 + z^2} = 1.1\}$.

The corresponding advection velocities are given as follows

- Sphere: $\mathbf{v} = 0.01 \hat{\mathbf{N}} \times (0, 0, -1)$,
- Torus: $\begin{cases} v_x = \rho_2 \cos(3\theta) - 3\rho_1 \sin(3\theta), \\ v_y = \rho_2 \sin(3\theta) + 3\rho_1 \cos(3\theta), \\ v_z = 2r \cos(2\phi), \end{cases}$
where $\rho = \sqrt{x^2 + y^2}$, $\theta = \frac{1}{3} \tan^{-1} \left(\frac{y}{x} \right)$, $\phi = \frac{1}{2} \tan^{-1} \left(\frac{z}{\rho - R} \right)$,
 $R = 1$, $r = \frac{1}{3}$, $\rho_1 = R + r \cos(2\phi)$, $\rho_2 = -2r \sin(2\phi)$,
- Bretzel2: $\mathbf{v} = 0.01 \hat{\mathbf{N}} \times (-1, 0, 0)$,
- CPD surface: $\mathbf{v} = 0.01 \hat{\mathbf{N}} \times (0, 1, 0)$,
- Point clouds: $\mathbf{v} = 0.01 \hat{\mathbf{N}} \times (0, 0, 1)$.

REFERENCES

- [1] M. BERTALMIO, L.-T. CHEN, S. OSHER, AND G. SAPIRO, *Variational Problems and Partial Differential Equations on Implicit Surfaces*, J. Comput. Phys., 174 (2001), pp. 759–780.
- [2] C. ELLIOTT AND B. STINNER, *Modeling and Computation of Two Phase Geometric Biomembranes Using Surface Finite Elements*, J. Comput. Phys., 229 (2010), pp. 6585–6612.
- [3] G. DZIUK AND C. ELLIOTT, *Finite Element Methods for Surface PDEs*, Acta Numer., 22 (2013), pp. 289–396.
- [4] M. OLSHANSKII AND X. XU, *A Trace Finite Element Method for PDEs on Evolving Surfaces*, SIAM J. Sci. Comput., 39 (2017), pp. A1301–A1319.
- [5] B. KOVACS, B. LI, C. LUBICH, AND C. GUERRA, *Convergence of Finite Elements on an Evolving Surface Driven by Diffusion on the Surface*, Numer. Math., 137 (2017), pp. 643–689.
- [6] X. XIAO, D. ZIHUAN, AND X. FENG, *A Positivity Preserving Characteristic Finite Element Method for Solving the Transport and Convection–Diffusion–Reaction Equations on General Surfaces*, Comput. Phys. Commun., 247 (2020), p. 106941.
- [7] Y. XIE, X. ZHAO, M. RUBINATO, AND Y. YU, *An Improved Meshfree Scheme Based on Radial Basis Functions for Solving Incompressible Navier–Stokes Equations*, Int. J. Numer. Meth. Fluids, 93 (2021), pp. 2842–2862.
- [8] Q. YAN, S. JIANG, AND J. HARLIM, *Kernel-Based Methods for Solving Time-Dependent Advection-Diffusion Equations on Manifolds*, J. Sci. Comput., 94 (2023), pp. 1–34.
- [9] A. PETRAS AND S. RUUTH, *PDEs on Moving Surfaces Via the Closest Point Method and a Modified Grid Based Particle Method*, J. Comput. Phys., 312 (2016), pp. 139–156.
- [10] V. SHANKAR, G. WRIGHT, AND A. NARAYAN, *A Robust Hyperviscosity Formulation for Stable RBF-FD Discretizations of Advection-Diffusion-Reaction Equations on Manifolds*, SIAM J. Sci. Comput., 42 (2020), pp. A2371–A2401.
- [11] V. SHANKAR, G. WRIGHT, AND A. FOGELSON, *An Efficient High-order Meshless Method for Advection-Diffusion Equations on Time-varying Irregular Domains*, J. Comput. Phys., 445 (2021), p. 110633.

- [12] Y. WANG, B.-S. WANG, L. LING, AND W. S. DON, *A Time-Continuous Embedding Method for Scalar Hyperbolic Conservation Laws on Manifolds*, J. Sci. Comput., 93 (2022).
- [13] C. K. HUNG AND S. LEUNG, *A Simple Embedding Method for Scalar Hyperbolic Conservation Laws on Implicit Surfaces*, SIAM J. Sci. Comput., 45 (2023), pp. A2813–A2835.
- [14] V. SHANKAR AND G. WRIGHT, *Mesh-free Semi-Lagrangian Methods for Transport on a Sphere Using Radial Basis Functions*, J. Comput. Phys., 366 (2018), pp. 170–190.
- [15] A. PETRAS, L. LING, AND S. RUUTH, *Meshfree Semi-Lagrangian Methods for Solving Surface Advection PDEs*, J. Sci. Comput., 93 (2022).
- [16] Y. LIU, Y. QIAO, AND X. FENG, *A Semi-Lagrangian Radial Basis Function Partition of Unity Closest Point Method for Advection-Diffusion Equations on Surfaces*, Comput. Math. Appl., 177 (2025), pp. 100–114.
- [17] H. RUI AND M. TABATA, *A Second Order Characteristic Finite Element Scheme for Convection-Diffusion Problems*, Numer. Math., 92 (2002), pp. 161–177.
- [18] A. BERMÚDEZ, M. R. NOGUEIRAS, AND C. VÁZQUEZ, *Numerical Analysis of Convection-Diffusion-Reaction Problems with Higher Order Characteristics/Finite Elements. Part I: Time Discretization*, SIAM J. Numer. Anal., 44 (2006), pp. 1829–1853.
- [19] O. DAVYDOV, *Error Bounds for a Least Squares Meshless Finite Difference Method on Closed Manifolds*, Adv. Comput. Math., 49 (2023), p. 48.
- [20] S. RUUTH AND B. MERRIMAN, *A Simple Embedding Method for Solving Partial Differential Equations on Surfaces*, J. Comput. Phys., 227 (2008), pp. 1943–1961.
- [21] M. CHEN, K. C. CHEUNG, AND L. LING, *A kernel-based least-squares collocation method for surface diffusion*, SIAM J. Numer. Anal., 61 (2023), pp. 1386–1404, <https://doi.org/10.1137/21M1444369>.
- [22] K. C. CHEUNG AND L. LING, *A Kernel-based Embedding Method and Convergence Analysis for Surfaces PDEs*, SIAM J. Sci. Comput., 40 (2018), pp. A266–A287.
- [23] A. QUARTERONI AND A. VALLI, *Numerical Approximation of Partial Differential Equations*, Springer Ser. Comput. Math., 23, Springer-Verlag, Berlin, 1994.
- [24] T. MÄRZ AND C. MACDONALD, *Calculus on Surfaces with General Closest Point Functions*, SIAM J. Numer. Anal., 50 (2012), pp. 3303–3328.
- [25] H. AMANN, *Ordinary Differential Equations: An Introduction to Nonlinear Analysis*, de Gruyter Stud. Math., 13, Walter de Gruyter, Berlin, 1990.
- [26] E. FUSELIER AND G. B. WRIGHT, *Scattered Data Interpolation on Embedded Submanifolds with Restricted Positive Definite Kernels: Sobolev Error Estimates*, SIAM Journal on Numerical Analysis, 50 (2012), pp. 1753–1776.
- [27] M. CHEN AND L. LING, *Extrinsic Meshless Collocation Methods for PDEs on Manifolds*, SIAM Journal on Numerical Analysis, 58 (2020), pp. 988–1007.
- [28] B. MATÉRN, *Spatial Variation*, vol. 36, Springer Science & Business Media, 2013.
- [29] P.-O. PERSSON AND G. STRANG, *A simple mesh generator in matlab*, SIAM Review, 46 (2004), pp. 329–345.
- [30] X. LI, *TBRBF method for advection-diffusion*. <https://github.com/LiXiaobin-code/trajectory-based-RBF-collocation-method-for-surface-advection-diffusion-equations->, 2025.
- [31] G. JIANG AND C. SHU, *Efficient Implementation of Weighted ENO Schemes*, Journal of computational physics, 126 (1996), pp. 202–228.